ARTICLE IN PRESS

Ceramics International xxx (xxxx) xxx

Contents lists available at ScienceDirect

Ceramics International

journal homepage: www.elsevier.com/locate/ceramint

Bioinspired synthesis of titania nanoparticles with enhanced crystallinity and tunable optoelectronic features

Nusrat Zahan, Md Rashed Alam, Munira Sultana, Afrina Sharmin, Shahran Ahmed, Sharmin Jahan, M.S. Bashar

Bangladesh Council of Scientific and Industrial Research (BCSIR), Dr. Qudrat-i-Khuda Road, Dhanmondi, Dhaka, 1205, Bangladesh

ARTICLE INFO

Handling Editor: Dr P. Vincenzini

Keywords:
Green synthesis
Sustainable nanoparticles
Neem leaf extract
Sol-gel method
Surface crystallinity

ABSTRACT

While green synthesis offers an eco-friendly route to titanium dioxide (TiO_2) nanoparticles, a lack of systematic parameter control often limits the ability to tailor their properties for specific applications. This study addresses this gap by comprehensively investigating the effects of neem leaf (Azadirachta indica) condition, solvent, and calcination temperature to establish a controllable synthesis framework. To assess the impact of different parameters, both fresh and dry neem leaves were extracted using ethanol, isopropanol, and acetonitrile solvents. The resulting nanoparticles were subjected to calcination at 500 °C and 900 °C to produce the anatase and rutile crystal phases, respectively. A comprehensive characterization was conducted employing techniques for analyzing their crystallographic, morphological, and photonic attributes. XRD analysis verified the purity of the crystalline phases, revealing the smallest crystallite size (11.85 nm) for nanoparticles synthesized using fresh leaves and ethanol. SEM imaging displayed consistently uniform, pseudo-spherical particles with particle sizes ranging from 75 to 80 nm at 500 °C and 80–95 nm at 900 °C, highlighting the effectiveness of the green synthesis method in achieving well-defined morphologies. EDS analysis confirmed a Ti:O stoichiometric ratio close to 1:2, affirming material purity. UV-DRS measurements demonstrated band gap energies between 3.18 and 3.31 eV at 500 °C and 3.08–3.11 eV at 900 °C, closely resembling those of chemically pure TiO_2, reinforcing the reliability of this synthesis route. Raman spectroscopy indicated that the nanoparticles produced using isopropanol exhibited superior surface crystallinity, accompanied by a notably low Urbach energy (~177 meV), suggesting a highly ordered structure with minimal defects. These findings underscore the potential of neem leaf extracts as an accessible, sustainable, and effective alternative for producing high-quality TiO_2 nanoparticles. Based on their tailored properties, these nanoparticles are expected to show potential for diverse applications, including photo catalysis, environmental remediation, and renewable energy technologies, contributing to the advancement of green chemistry and sustainable nanomaterials.

1. Introduction

The development of sustainable and controllable methods for producing nanomaterials with tailored properties is a critical challenge in modern materials science. While green synthesis using plant extracts offers an eco-friendly alternative to conventional routes, a systematic understanding of how to control the final nanoparticle characteristics is often lacking [1]. Nanotechnology encompasses a wide array of applications across various fields due to its unique characteristics at the nanoscale, such as size, structure, and physicochemical and biological properties. These applications extend to numerous industries, including mechanical and electronic engineering, imaging for targeted therapy, and molecular diagnostics [2]. A variety of nanoparticles, such as titanium dioxide (TiO_2), tin dioxide (SnO_2), zinc oxide (ZnO), cadmium sulfide (CdS), and cerium dioxide (CeO_2) are synthesized owing to their unique optical, electronic, and catalytic characteristics [3]. Among them TiO_2 is the most prominent photocatalyst for breaking down organic contaminants and antibiotics for its strong photocatalytic performance, great energy efficiency, cost effectivity, non-toxicity, and high stability [4]. The performance of TiO_2 in these roles is directly governed by its physical properties. For example, a smaller nanoparticle size creates a larger surface-area-to-volume ratio, providing more active sites for catalysis and thereby improving the efficiency of processes like the degradation of organic pollutants in wastewater [5]. Furthermore, the

* Corresponding author.
E-mail addresses: bashar@agni.com, bashar@bcsir.gov.bd (M.S. Bashar).

https://doi.org/10.1016/j.ceramint.2025.07.318
Received 4 May 2025; Received in revised form 9 July 2025; Accepted 22 July 2025
Available online 5 August 2025

Please cite this article as: Nusrat Zahan et al., *Ceramics International*, https://doi.org/10.1016/j.ceramint.2025.07.318

crystal phase is paramount; the anatase phase is renowned for its high photocatalytic activity, making it ideal for environmental remediation, while the more stable rutile phase is the industry standard for pigments and sunscreens due to its superior light-scattering and UV-protection capabilities. Therefore, a synthesis method that allows for precise control over these fundamental properties is essential for developing nanomaterials tailored for high-performance, real-world applications [6,7]. Different types of techniques are available for synthesis of TiO_2 nano particles, those are Solution Combustion [8], Sol-Gel [9], Hydrothermal [10], Solvo-thermal [11], Chemical Vapor Deposition [12] and Green synthesis [13]. However, many of these conventional methods often involve harsh reaction conditions, such as high temperatures and pressures, or the use of toxic and environmentally hazardous chemicals [14]. Consequently, establishing a simple, low-cost, and eco-friendly synthesis route that offers precise control over the final nanoparticle properties is a highly desirable goal in materials chemistry [15].

However, the chemical process uses artificial agents for capping, reducing, and stabilizing, which leads to the production of byproducts that are not sustainable for the environment whereas green synthesis generally uses natural and non-toxic reducing and stabilizing agents like plant extracts, which greatly lessen the environmental impact compared to conventional chemical methods [16]. Green synthesis methods are capable of producing nanoparticles with more uniform size distribution and enhanced control over morphology, which is especially crucial for applications in medicine, catalysis, and environmental science [17]. Besides, nanoparticles produced through green synthesis methods tend to be more biocompatible, which enhances their suitability for biomedical uses like drug delivery, biosensors, and medical imaging [18]. However, a significant challenge in green synthesis is achieving consistent control over the nanoparticle's fundamental properties—such as crystal phase, size, and crystallinity—which are often highly sensitive to variations in the plant extract and synthesis conditions [19]. In particular, achieving selective synthesis of a pure crystalline phase—either the photocatalytically superior anatase or the thermally stable rutile—without phase mixtures often remains a difficult objective for simple, low-temperature green routes [20].

There is extensive literature documenting the production of green nanomaterials such as gold (Au), copper (Cu), silver (Ag), titanium dioxide (TiO_2), zinc oxide (ZnO), copper oxide (CuO), iron oxide (Fe_3O_4), and tin dioxide (SnO_2), nanoparticles [21]. These eco-friendly synthesis techniques employ plant extracts and other sustainable methods, presenting possible uses in cytotoxicity, larvicidal effects, antimicrobial properties, and photocatalysis [21]. Recently, green TiO_2 nanostructures have been fabricated utilizing plant extracts like Nyctanthes arbor-trists extract [22], Latex of Jatrophacurcas L. [23], Aloe barbadensis leaves extract [24], Psidium guajava leaves extract [25] etc. The literature survey revealed significant potential for biosynthesis of TiO_2 nanoparticles. Specifically, utilizing leaf extracts streamlines the large-scale production of nanoparticles more effectively than other biological sources such as bacteria and fungi [21]. However, many of these studies focus on a single set of synthesis conditions, leaving a gap in the systematic, side-by-side comparison of key variables needed to understand the trade-offs in tailoring nanoparticle properties.

Despite the extensive investigation into green synthesis techniques for various nanomaterials, the application of neem leaf extract for the biochemical synthesis of titanium dioxide (TiO_2) nanoparticles has received comparatively limited attention. This study specifically adopts the biosynthetic approach due to its distinct advantages over conventional chemical methods. Unlike chemical synthesis, which frequently involves toxic reagents and produces environmentally hazardous byproducts, biosynthesis leverages natural, non-toxic materials, aligning with the principles of green chemistry. This makes the process inherently more sustainable and safer for applications in biomedical and environmental fields.

Neem (Azadirachta indica) leaves, rich in bio-functional molecules like alkaloids, coumarins, and flavonoid antioxidants, provide a s sustainable replacement to traditional synthetic routes [1]. The various functional groups present in these phytochemicals, such as hydroxyls and carbonyls, are believed to serve as effective reducing and capping agents, which first reduce the metal precursor and then stabilize the newly formed nanoparticles to control their growth [26]. These bioactive constituents serve as natural reductants and stabilizers, removing the necessity for harmful reagents, thereby minimizing environmental impact and improving biocompatibility [1].

While the field of green nanomaterial synthesis is rapidly expanding, most studies focus on a single set of parameters. A significant gap remains in the systematic optimization and comparative analysis of key synthesis variables within a single framework. Specifically, the combined and distinct effects of precursor condition (fresh vs. dry leaves), solvent polarity, and calcination temperature on the properties of neem-synthesized TiO_2 nanoparticles have not been thoroughly and concurrently compared. This research distinguishes itself by offering precisely this detailed comparative analysis. By systematically varying the neem leaf condition, the extraction solvent (ethanol, isopropanol, and acetonitrile), and the calcination temperature (500 °C and 900 °C), we aim to elucidate how these variables govern the final nanoparticle crystallinity, phase structure, morphology, and optical behavior, thereby providing a clear roadmap for tailoring nanoparticle properties for specific applications. Employing neem (Azadirachta indica) leaf extract—a potent natural source of reducing and capping agents like flavonoids and antioxidants, often underutilized—this study demonstrates a viable, sustainable, and scalable approach to producing TiO_2 nanoparticles with tailored features. This research emphasizes the transformative opportunity of biosynthetic methods in nanotechnology, particularly for producing nanoparticles with tailored properties that are desirable for applications in medicine, catalysis, and environmental remediation. The study's novelty is further underscored by its exploration of multiple solvent systems (ethanol, isopropanol, acetonitrile) in conjunction with both fresh and dry leaf precursors, facilitating a rare examination of solvent-phytochemical interactions during synthesis. Moreover, we demonstrate effective thermal control over phase composition, selectively producing anatase (500 °C) and rutile (900 °C) TiO_2. This phase control, elucidated through in-depth characterization using XRD, Raman spectroscopy, SEM, EDS, and UV-DRS, offers crucial structure-property correlations for optimizing nanoparticles for specific functional roles. While this work contributes to the understanding of green-synthesized TiO_2 nanoparticles, its scope has inherent limitations. The investigation prioritized physical characterization, leaving the specific mechanistic contributions of phytochemicals during nanoparticle nucleation and growth largely unexplored. Additionally, experimental validation of the material's photocatalytic activity and assessment of its viability for practical applications were not undertaken. Furthermore, the present study identifies several promising synthesis routes such as those utilizing ethanol for minimal crystallite size or isopropanol for high structural order which now warrant the focused, in-depth performance analysis suggested for future work. Future studies should also incorporate advanced characterization techniques, such as BET analysis to quantify surface area and porosity, Transmission Electron Microscopy (TEM) for higher-resolution morphological and crystallinity assessment, and X-ray Photoelectron Spectroscopy (XPS) to investigate surface chemical states. In addition, a detailed mechanistic study would benefit from GC-MS analysis of the leaf extracts to identify the specific active compounds and TGA-DSC analysis to precisely monitor the thermal decomposition and phase transition processes.

2. Experimental design

2.1. Fabrication of nanoparticles

The green synthesis of TiO_2 nanoparticles was achieved through a sol-gel procedure, proceeded by a calcination operation. Fig. 2.1 illustrates the synthesis route employed for producing TiO_2 nanoparticles.

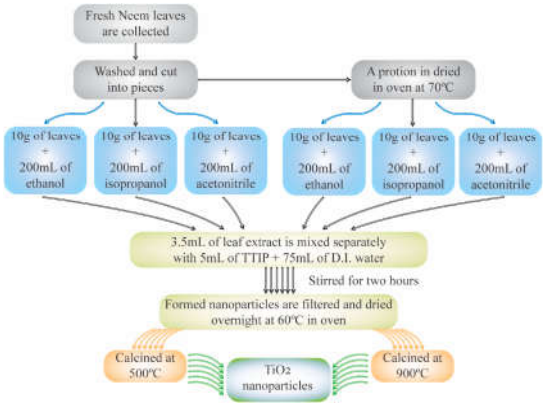

Fig. 2.1. Synthesis route of TiO_2 nanoparticles.

Neem leaves in good condition were collected from the BCSIR campus in Dhaka, Bangladesh. The leaves were thoroughly washed to remove dust and cut into pieces. A portion of the leaves were dried in the oven at 70 °C. Ten grams of both fresh and dry leaves were mixed separately with 200 mL of ethanol, 200 mL of isopropanol, and 200 mL of acetonitrile and kept overnight. Later the combination was subjected to filtration using Whatmann filter paper to yield the neem leaf extract in ethanol, isopropanol and acetonitrile respectively. These extracts were then utilized to synthesize TiO_2 nanoparticles.

To synthesize the TiO_2 nanoparticles, a beaker containing 5 mL of titanium isopropoxide (TTIP) was blended with 3.5 mL of the ethanolic leaf extract (both fresh and dry) and 75 mL of deionized water. The combination was agitated continuously with a stirring magnet at ambient temperature. The synthesis of TiO_2 nanoparticles via this sol-gel process involves two primary chemical reactions: hydrolysis and condensation [27].

1. **Hydrolysis:** First, the isopropoxide groups (–O-iPr) on the titanium precursor react with water and are replaced by hydroxyl groups (–OH). This reaction can be represented as:

$$Ti(O\text{-}iPr)_4 + H_2O \rightarrow Ti(OH)(O\text{-}iPr)_3 + iPr\text{-}OH$$

This hydrolysis step continues, progressively replacing the isopropoxide groups.

2. **Condensation:** Next, the hydroxylated precursor molecules link together to form stable Ti-O-Ti bridges, creating the solid gel network. This occurs through two main pathways:

Oxolation: Two hydroxyl groups react, releasing a water molecule.

$$(Ti\text{-}O\text{-})_3Ti\text{-}OH + HO\text{-}Ti(\text{-}O\text{-}Ti)_3 \rightarrow (Ti\text{-}O\text{-})_3Ti\text{-}O\text{-}Ti(\text{-}O\text{-}Ti)_3 + H_2O$$

Alcoxolation: A hydroxyl group reacts with a remaining isopropoxide group, releasing an isopropanol molecule.

$$(Ti\text{-}O\text{-})_3Ti\text{-}OH + iPr\text{-}O\text{-}Ti(\text{-}O\text{-}Ti)_3 \rightarrow (Ti\text{-}O\text{-})_3Ti\text{-}O\text{-}Ti(\text{-}O\text{-}Ti)_3 + iPr\text{-}O$$

These reactions build the three-dimensional titania network, while the phytochemicals from the neem extract adsorb onto the surface, controlling particle size and preventing aggregation [27]. After 2 h of stirring, the resulting TiO_2 nanoparticles were collected and initially dried in an oven at 60 °C overnight. The dried samples were then subjected to further heat treatment in a muffle furnace for about 3 h at both 500 °C and 900 °C to form TiO_2 powder. The same procedure was followed for synthesizing TiO_2 nanoparticles using the neem leaf extracts obtained with isopropanol and acetonitrile. Each solvent was tested with both fresh and dry neem leaves, and the final TiO_2 powders were calcined at the same temperatures for comparative analysis.

Twelve different TiO_2 nanoparticle samples were synthesized using neem leaf extract (dry and fresh) with ethanol, isopropyl alcohol, and acetonitrile as solvents. The synthesized samples were then calcined at two distinct temperatures, 500 °C and 900 °C. This systematic design is essential for the study's primary objective: to de-convolute the specific effects of each parameter and to draw meaningful conclusions from their direct comparison under controlled conditions. The information of the samples synthesized based on the specific conditions is listed in Table 2.1. The sample codes are systematic: 'S' denotes the sample, the first letter indicates the leaf type ('F' for Fresh, 'D' for Dry), and the second letter indicates the solvent ('E' for Ethanol, 'I' for Isopropanol, 'A' for Acetonitrile), and the final number represents the calcination temperature ('5' for 500 °C and '9' for 900 °C.

2.2. Characterization techniques

The synthesized TiO_2 nanoparticles were characterized using various analytical techniques to determine their structural, morphological, and elemental properties. X-ray diffraction (XRD) analysis was performed to ascertain the crystal structures and assess the crystallite sizes of the TiO_2

Table 2.1
List of samples synthesized at different conditions.

Sample name	Leaf type	Solvent type	Calcination temperature (°C)
S-FE5	Fresh	Ethanol	500
S-FE9	Fresh	Ethanol	900
S-DE5	Dry	Ethanol	500
S-DE9	Dry	Ethanol	900
S-FI5	Fresh	Isopropanol	500
S-FI9	Fresh	Isopropanol	900
S-DI5	Dry	Isopropanol	500
S-DI9	Dry	Isopropanol	900
S-FA5	Fresh	Acetonitrile	500
S-FA9	Fresh	Acetonitrile	900
S-DA5	Dry	Acetonitrile	500
S-DA9	Dry	Acetonitrile	900

nanoparticles. An EMMA X-ray diffractometer (GBC Corporation, Australia) was used to record the XRD patterns, utilizing Cu-Kα X-ray emission having a wavelength of 1.5406 Å. The equipment was controlled at 35 kV and 28 mA. The scattering patterns were compiled over a 2θ interval of 10°–80° with a step size of 0.05° and a counting time of 2s per step. Rietveld refinement was applied to the XRD data to obtain precise lattice parameters and crystallite sizes. The morphology was inspected by scanning electron microscopy (SEM; EVO18, Carl Zeiss, UK), which was operated at an accelerating voltage of 25 kV. SEM analysis provided detailed images of the surface configuration and particulate size of the TiO_2 nanoparticles. The particle size distribution of the TiO_2 nanoparticles was measured using ImageJ software. The particle size distribution graphs were plotted to visualize the variation in particle sizes under different synthesis conditions. Energy-dispersive X-ray (EDS) spectroscopy was utilized to examine the elemental content of the TiO_2 nanoparticles, employing a Team EDS system (EDAX, AMETEK, USA; beam voltage: 15 kV) connected to the SEM unit. Elemental mapping was also carried out using this system to visualize the spatial distribution of the constituent elements. Raman spectroscopy (LabRAM HR Evolution, Horiba Scientific, Japan) is utilized to capture the distinct molecular signature of the compounds. An UV–visible (UV–Vis) spectrophotometer (UH4150, Hitachi, Japan) was employed to analyze the optical absorbance and evaluate the band gap energies at visible wavelengths. The Fourier Transform Infrared (FTIR) spectrometer operated under the following parameter settings- 8400S spectrophotometer, Shimadzu, Japan): wavenumber range: 4000–400 cm−1; resolution: 4 cm−1; scans: 30.

3. Result and insights

3.1. Structural features

The XRD patterns of TiO_2 nanoparticles synthesized using both dry and fresh neem leaf extracts in ethanol, isopropyl alcohol, and acetonitrile solvents and calcined at both 500 °C and 900 °C are shown in Fig. 3.1(a, b), 3.2(a, b, c) and 3.3(a, b). In this study, all samples were calcined at 500 °C and 900 °C to obtain the anatase and rutile phases of TiO_2, respectively. The anatase phase typically forms at lower calcination temperatures (around 500 °C), while the rutile phase develops at higher temperatures (approximately 900 °C) [28]. Both phases were deliberately targeted owing to their distinctive characteristics and versatile implementations in diverse areas. Anatase is well-known for its excellent photocatalytic performance, making it optimal for implementations in environmental restoration and energy management [29]. Conversely, rutile, characterized by its greater thermal stability and higher refractive index, is widely used in coatings, pigments, and optical devices [30]. By synthesizing both phases, this study ensures the TiO_2 nanoparticles have enhanced versatility to meet diverse industrial and research requirements.

For the samples calcined at 500 °C, all curves show the characteristic peaks of the anatase phase. Taking sample S-FE5(fresh leaf, ethanol solvent, 500 °C) as a representative example, the dominant diffraction peaks observed at 2θ values of 25.3°, 37.8°, 48.0°, 53.9°, 55.0° and 62.7° correspond to the (101), (004), (020), (105), (121) and (024) planes of anatase TiO_2 i.e., Crystallography Open Database (COD) card no. 96-900-9087, respectively (Inset of Fig. 3.1a) and are consistent with existing literature [31]. These peaks reveal that the anatase phase is the predominant phase present in the samples calcined at this temperature and no extraneous peak is detected, demonstrating the authenticity of TiO_2.

Upon increasing the calcination temperature to 900 °C, a clear phase transition to rutile is observed. Using sample S-FE9 (fresh leaf, ethanol solvent, 900 °C) as a representative example, additional peaks corresponding to the rutile phase of TiO_2 i.e., COD card no. 96-900-4143, were observed at 2θ values of 27.4°, 36.1°, 41.2°, 54.2°, and 56.5° corresponding to the (110), (101), (111), (211), and (220) planes, respectively (Inset of Fig. 3.1b) and are consistent with existing study [32]. This indicates a phase transition from anatase to rutile at higher calcination temperatures.

Rietveld refinement was performed on the XRD data to quantify the phase composition and to obtain detailed information on the crystal structure parameters. The refinement process involved fitting the entire XRD pattern using the FullProf software, and the quality of the fit was assessed by the R-factors and the χ^2 values. The D-spacing between atoms (d-spacing) has been acquired through Rietveld refinement.

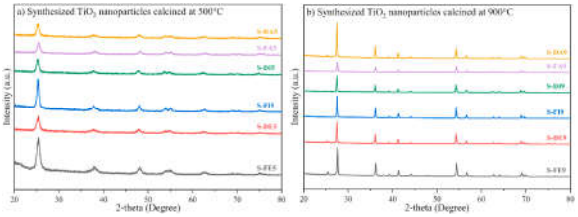

Fig. 3.1. Powder X-ray diffraction patterns TiO_2 nanoparticles (a. calcined at 500 °C; b. calcined at 900 °C) for both fresh and dry neem leaf using ethanol, isopropanol and acetone as extraction solvent.

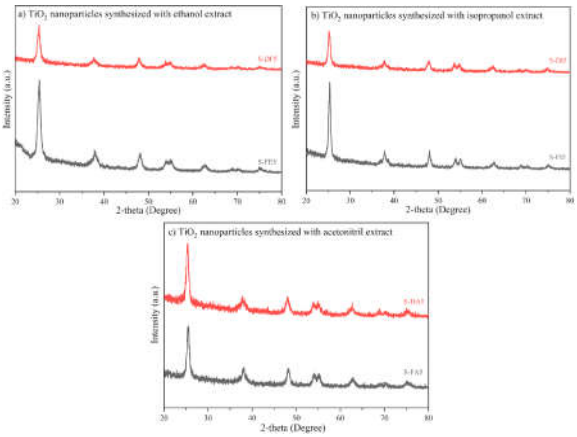

Fig. 3.2. Powder X-ray diffraction patterns TiO_2 nanoparticles calcined at 500 °C for both fresh and dry neem leaf (using a. ethanol as an extraction solvent; b. isopropanol as an extraction solvent; c. acetone as extraction solvent).

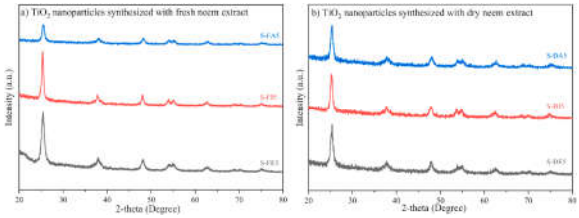

Fig. 3.3. Powder X-ray diffraction patterns TiO_2 nanoparticles calcined at 500 °C using ethanol, isopropanol and acetone as extraction solvent (for a. fresh neem leaf; b. and dry neem leaf).

Additionally, the refined lattice parameters for the anatase phase were found to be around, a = b = 3.7999 Å, c = 9.5291 Å, and for the rutile phase, they were a = b = 4.60300 Å, c = 2.96600 Å. In comparison, the unrefined lattice parameters for the anatase phase were around a = 3.7850 Å, c = 9.5140 Å and for the rutile phase, they were a = 4.6030 Å, c = 2.9660 Å. The weight fractions of anatase and rutile phases were determined to be 100 % anatase for the samples calcined at 500 °C and 100 % rutile for the samples calcined at 900 °C. The slight differences in the lattice parameters between the refined and unrefined results highlight the importance of Rietveld refinement in providing more accurate and detailed crystal structure information. The Rietveld refinement results verified the successful synthesis of TiO_2 nanoparticles with controlled phase composition, ensuring a more precise characterization of the anatase and rutile phases.

Fig. 3.1(a and b) show the characteristic peaks of the nanoparticles calcined at 500 °C and 900 °C. The intensity of the characteristic peak for the nanoparticles calcined at 900 °C is higher than that for those calcined at 500 °C, with the peaks being much sharper in the latter case. This can be attributed to several factors related to the crystallinity and particle size of the nanoparticles. Calcination at elevated temperatures enhances crystallinity and promotes the formation of larger crystallites [33]. As the temperature rises, smaller crystallites combine to create

larger ones. These larger crystallites scatter X-rays more uniformly, leading to sharper and more pronounced peaks in the XRD pattern [33]. Additionally, higher temperatures can relieve internal strains within the nanoparticles, as strain in the crystal lattice can cause peak broadening in XRD patterns [34]. By calcining at 900 °C, the strain is reduced, resulting in narrower and more intense peaks [34].

The comparison of the intensity of characteristic peaks for nanoparticles synthesized using fresh and dry neem leaves, both calcined at 500 °C, is illustrated in Fig. 3.2(a, b, c). The figures indicate that nanoparticles derived from fresh leaves exhibit higher peak intensities compared to those from dry leaves when ethanol and isopropanol are used as extraction solvents. However, with acetonitrile as the solvent, nanoparticles from dry neem leaves show higher peak intensities. Plausible explanations for the observed differences in XRD peak intensities and sharpness include factors such as the interaction between the solvent and the varying phytochemical composition of fresh versus dry leaves. Fresh neem leaves have higher volatile organic compounds and water content than dry leaves, which can perform as reductants and stabilizers during synthesis. In the case of acetonitrile, a strong solvent, the extraction efficiency of these compounds may be higher with dry leaves, leading to improved crystallinity and sharper peaks [35]. Another factor could be that acetonitrile has different polarity and solvent properties compared to ethanol and isopropanol, leading to varied interactions with the phytochemicals in fresh and dry neem leaves. Acetonitrile may extract more stable and effective compounds from dry neem leaves for nanoparticle formation, resulting in sharper XRD peaks [36].

Fig. 3.3(a and b) present a comparison of the intensity of characteristic peaks for nanoparticles synthesized from fresh and dry neem leaves, using ethanol, isopropanol, and acetonitrile as extraction solvents, all calcined at 500 °C. The results indicate that nanoparticles synthesized with ethanol exhibit the highest peak intensity and sharpness, indicating superior crystallinity for both fresh and dry neem leaves. Peaks for nanoparticles prepared with isopropanol show slightly lower intensity compared to those with ethanol. Peaks for nanoparticles synthesized with acetonitrile have the lowest intensity, reflecting the lowest crystallinity among the solvents used. These variations in peak intensity and crystallinity can be mechanistically linked to the interaction between the solvents and the bioactive compounds in the neem leaf extract. Neem leaves are rich in compounds like flavonoids and terpenoids, which are known to be effective in nanoparticle synthesis. The hydroxyl groups of flavonoids, for instance, can act as powerful reducing agents for the titanium precursor and as capping agents that control particle growth by chelating the nanoparticle surface [37]. Ethanol, with its stronger reducing power compared to isopropanol and acetonitrile, can more effectively reduce metal ions, leading to nanoparticles with higher crystallinity and sharper peaks [38]. In contrast, while acetonitrile is polar, it is less polar than ethanol and isopropanol. This reduced polarity may result in poorer solubility of the precursor materials and weaker interactions with the neem leaf extract, leading to less uniform and less well-defined nanoparticles, which in turn results in lower crystallinity and less sharp peaks. The influence of the neem extract on the nanoparticle properties can be explained by the mechanistic role of its constituent phytochemicals, such as flavonoids and terpenoids. During the initial nucleation stage, the abundant hydroxyl and carbonyl groups on these molecules can chelate the titanium ions, acting as centers for the formation of the initial TiO_2 nuclei [39]. As the nanoparticles begin to form through the sol-gel process, these large organic molecules adsorb onto the surface, serving as natural capping agents. This layer sterically hinders uncontrolled particle growth and prevents aggregation, allowing for the formation of smaller and more uniform nanoparticles [40]. The quality of this capping layer, which is influenced by the solvent's ability to extract these active compounds, directly impacts the crystallinity and defect formation. A more effective capping layer, such as that likely formed using the ethanol extract, can lead to a more ordered crystal growth process, resulting in higher crystallinity and fewer lattice defects [40].

The average crystallite size of the fabricated nanoparticles was evaluated by using both the Debye-Scherrer (D-S) and Williamson-Hall (W-H) plots shown in Fig. 3.4 [9,41].

$$D = \frac{K\lambda}{\beta \cos\theta}; \quad (1)$$

Where, D = Average crystal size, K = Debye-Sherrer's constant (shape factor, about 0.9), λ = wavelength of the X-Ray (0.15418 nm), β = Full width at half maximum (FWHM) of the diffraction line and θ = Diffraction angle.

$$\beta \cos\theta = 4\varepsilon \sin\theta + \frac{k\lambda}{D}; \quad (2a)$$

Where, ε resembles lattice strain. The average crystal dimension of the synthesized nanoparticles revealed an increase in particle size with elevating calcination temperature, as shown in Table 3.1. For the samples calcined at 500 °C, the crystallite size averaged at 10–20 nm (D-S) and 10–24 nm (W-H), while for those calcined at 900 °C, it increased to 45–60 nm (D-S) and 57–62 nm (W-H), respectively. The good agreement between the two models validates the calculated nanoscale dimensions and the effect of temperature on crystal growth. From Tables 3.1 and it is evident that sample S-FE5 (fresh leaves, ethanol, and 500 °C), has the smallest crystal size and the highest crystallinity, which is observed from the XRD analysis. These traits are considered highly desirable for applications that depend on surface area, charge mobility, and photocatalytic efficiency [42]. Therefore, this synthesis method provides the most favorable material properties for advanced applications, especially in comparison to other solvent and leaf extract combinations.

3.2. Morphology

Scanning Electron Microscopy (SEM) was conducted at a magnification of 50,000x −100,000x. The corresponding SEM images and particle size distribution graph are demonstrated in Fig. 3.5(a–l). The SEM images revealed that the nanoparticles exhibited a pseudo-spherical morphology and were generally well-dispersed with minimal agglomeration, which are characteristic and desirable features for nanoparticles synthesized through green methods [43].

Particle size measurements were conducted using ImageJ software, and the size distribution curves were plotted accordingly. Comparative analysis of the SEM images of the nanoparticles calcined at distinct temperatures highlighted the morphological changes induced by the calcination process. For samples calcined at 500 °C, the particle sizes ranged between 75 and 80 nm, while for samples calcined at 900 °C, the particle sizes varied between 80 and 95 nm. The increase in particle size with higher calcination temperatures can be attributed to the sintering effect [44]. During sintering, particles coalesce and grow due to increased atomic and ionic mobility, facilitated by elevated temperatures [44]. Mechanisms like Ostwald ripening and grain boundary diffusion contribute to this phenomenon.

The SEM images at various magnifications offered a detailed and comprehensive depiction of the surface morphology of the nanoparticles. This reduced agglomeration leads to increased surface area, which is advantageous for catalytic and adsorption applications [45,46]. The pseudo-spherical shape and uniform size distribution further validate the effective synthesis of TiO_2 nanoparticles through the use of neem leaf extract. The findings from the SEM analysis underscore the effectiveness of neem leaf extract as a reductant and stabilizer in the green fabrication of TiO_2 nanoparticles. Moreover, the calcination process's impact on particle size and morphology provides insights into optimizing synthesis parameters for desired nanoparticle characteristics.

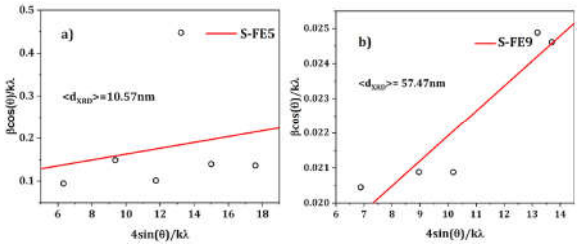

Figure-3.4. Williamson-Hall (W–H) plots for determining the crystallite size of representative samples S-FE5 (synthesized using fresh leaves and ethanol and calcined at 500 °C) and S-FE9 (synthesized under the same conditions but calcined at 900 °C).

Table 3.1
Crystallite properties of the nanoparticles from XRD.

Nanoparticles	Calcination Temp. (°C)	Crystal phase	Average crystallite size (D-S) (nm)	Average crystallite size (W-H) (nm)	Lattice parameters (Å) (Refined)		Volume (Å)^3
					a	c	
S-FE5	500	Anatase (100 %)	11.85	10.57	3.79	9.51	136.72
S-FE9	900	Rutile (100 %)	51.50	57.47	4.60	2.97	62.85
S-DE5	500	Anatase (100 %)	13.70	11.28	3.80	9.52	137.47
S-DE9	900	Rutile (100 %)	48.60	61.76	4.60	2.96	62.61
S-FI5	500	Anatase (100 %)	13.10	17.18	3.79	9.52	136.65
S-FI9	900	Rutile (100 %)	44.90	56.98	4.61	2.97	62.96
S-DI5	500	Anatase (100 %)	17.43	19.83	3.80	9.54	138.01
S-DI9	900	Rutile (100 %)	46.00	54.18	4.60	2.97	62.85
S-FA5	500	Anatase (100 %)	18.90	22.54	3.79	9.52	136.99
S-FA9	900	Rutile (100 %)	55.61	60.49	4.60	2.97	62.89
S-DA5	500	Anatase (100 %)	19.00	23.39	3.79	9.51	136.67
S-DA9	900	Rutile (100 %)	56.19	61.78	4.60	2.96	62.70

3.3. Composition analysis

The EDS spectra for two samples calcined at 500 °C and 900 °C respectively, are shown in Fig. 3.6(a and b).

For nanoparticles calcined at 500 °C, the EDS analysis (Fig. 3.6a) detected Ti and O, which is consistent with the expected TiO_2 composition. Additionally, C and K were also observed in the EDS spectrum. The detected C and K are likely remnants of the organic phytochemicals (e.g., flavonoids, alkaloids) and inorganic salts from the neem leaf extract. These organic molecules are believed to serve as critical capping agents, adsorbing to the nanoparticle surface via hydroxyl or carbonyl groups to prevent agglomeration during synthesis [47]. In contrast, the EDS spectra of nanoparticles calcined at 900 °C showed only Ti and O. The absence of C and K at this higher temperature suggests that the calcination process at 900 °C eliminates these extraneous elements. No additional peaks from other elements were detected, indicating the formation of pure nanoparticles. The elemental percentages listed in Table 3.2 further support the nanoparticles' purity. The atomic ratio of Ti:O for the synthesized samples was consistently close to the ideal stoichiometric value of 1:2, as expected for TiO_2. This result indicates that the green synthesis method employed, utilizing neem leaf extract, successfully yielded TiO_2 with minimal deviations in composition. However, EDS analysis can only provide an estimation of the elements present in the materials, rather than their exact quantities [3].

3.3.1. Elemental mapping analysis

To further investigate the compositional homogeneity of the synthesized nanoparticles, EDS elemental mapping was performed on representative samples calcined at 500 °C and 900 °C, with the results shown in Fig. 3.7. The maps for the sample calcined at 500 °C reveal a uniform and overlapping distribution of titanium (Ti) and oxygen (O) across the entire scanned area.

For the sample calcined at 900 °C, the mapping likewise shows a dense and uniform distribution of only Ti and O. For both samples, the mapping confirms the absence of any localized clusters of impurities, providing strong evidence for the formation of a homogeneous TiO_2 material.

3.4. Raman analysis

Raman spectroscopy is a versatile and non-destructive tool commonly utilized for phase identification, structural analysis, and defect assessment in materials [48]. In this work, Raman spectra were used to validate the crystallographic phases of green-synthesized TiO_2 nanoparticles calcined at 500 °C and 900 °C, as illustrated in Fig. 3.8(a and b).

The Raman spectra of the samples calcined at 500 °C (Fig. 3.8 (a)) revealed four prominent peaks at 144, 197, 397, 516, and 639 cm^{-1}, attributed to the Eg, Eg, B1g, Eg, and Eg vibrational modes, respectively [49]. These peaks are distinct markers of the anatase phase, with no evidence of secondary phases or impurities, underscoring the samples phase consistency. The intensity variations among the samples highlight differences in crystallinity; the samples synthesized using isopropanol (e.g., S-FI5 and S-DI5) demonstrated the highest peak intensities,

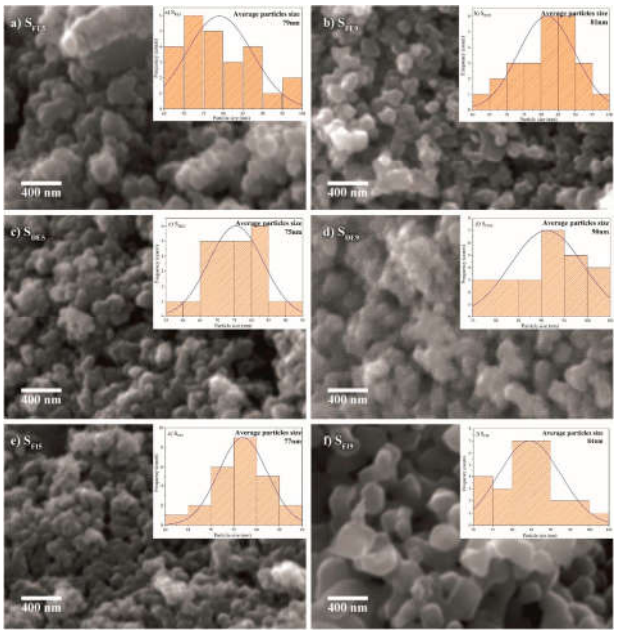

Fig. 3.5. SEM image of TiO_2 nanoparticles synthesized at different conditions.

indicating superior structural order and crystallinity. In contrast, the samples synthesized with ethanol displayed the lowest peak intensities, suggesting relatively lower crystallinity.

For the samples calcined at 900 °C, the Raman spectra (Fig. 3.8(b)) exhibited characteristic peaks at 143, 237, 447, and 612 cm^{-1}, which can be attributed to the B1g, Eg, B1g, and A1g vibrational modes respectively which are consistent with the expected Raman-active modes for rutile TiO_2 [50]. Since the spectra clearly showed overlapping features from a secondary phase, deconvolution analysis was performed to accurately resolve the individual peaks and quantify the phase composition. This deconvolution confirmed the presence of a subtle residual anatase phase, primarily through its characteristic B_1g peak at ~400 cm^{-1} (as detailed in the deconvoluted spectrum in Fig. 3.9).

The phase percentage was calculated from the integrated areas (IA for anatase and IR for rutile) obtained via deconvolution using the following equations [51]:

$$\text{Phase \% of anatse} = \frac{IA}{(IA + IR)}\ x\ 100; \tag{2b}$$

$$\text{Phase \% of rutile} = \frac{IR}{(IA + IR)}\ x\ 100; \tag{3}$$

Where, I_A is the peak intensity corresponding to the anatase phase, and I_R is the peak intensity corresponding to the rutile phase. The calculated phase percentages for the anatase and rutile phases were presented in Table 3.3.

A subtle residual peak corresponding to the anatase phase was observed at 144 cm^{-1}, particularly in the samples synthesized with ethanol, suggesting the presence of a small amount of anatase. Phase percentage calculations indicated that the samples synthesized with ethanol retained a higher proportion of anatase compared to those synthesized with acetonitrile. In contrast, the samples synthesized with isopropanol exhibited the lowest anatase content, which is consistent

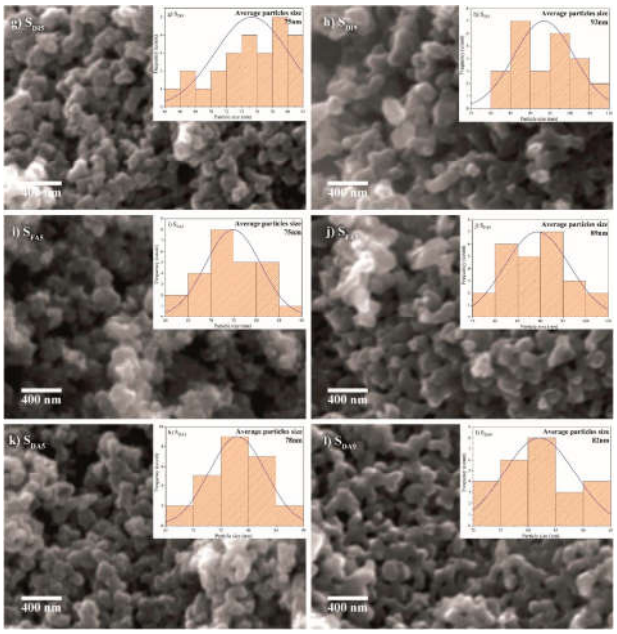

Fig. 3.5. (*continued*).

with their near-complete transformation to the rutile phase.

The variations in peak intensities and anatase content can likely be attributed to the type of solvent used, as it influences the crystallization process and phase stability during calcination [52] These results highlight the significant impact of synthesis conditions on the phase composition and crystallinity of TiO_2 nanoparticles. Notably, although the XRD analysis indicated that samples synthesized with ethanol exhibited the highest peak intensities at both calcination temperatures, this pattern was not observed in the Raman spectra. This inconsistency may be attributed to the differing sensitivities of the two techniques: XRD primarily assesses bulk crystallinity, while Raman spectroscopy is more sensitive to surface characteristics, potentially capturing localized variations in phase distribution or crystal orientation [53,54].

3.5. Optical characteristics evaluation

The optical characteristics of the TiO_2 nanoparticles synthesized through green methods were examined using UV–Vis diffuse reflectance spectroscopy (UV-DRS) from 300 nm to 800 nm. The findings are displayed in Fig. 3.10(a and b), showing a sharp decline in absorbance around 416 nm for all nanoparticle samples calcined at 500 °C and 900 °C temperatures. The band gap energy (Eg) was calculated from the Tauc plot, derived from the reflectance data using the Kubelka-Munk function [3].

$$F(R) = \frac{K}{S} = \frac{(1-R)^2}{2R}; \tag{4}$$

F(R) is proportional to the ratio of the absorption coefficient (K) to the back scattering factor (S) of the material [55]. R represents reflectance. Given that, the absorption coefficient of the sample K is, $K = \frac{4\pi k}{\lambda}$; where λ is the wavelength of the absorbed photon, and k is the spectral extinction co-efficient [3]. The band gap of the composites can be evaluated from the Tauc equation by extending the linear portion of the plot, where $(\alpha h\upsilon)^{1/n}$ is plotted on the y-axis and photon energy ($h\upsilon$) is on the x-axis (Fig. 3.10(c and d)). The bandgap in the optical range is then identified by extending this linear region until it intersects the x-axis.

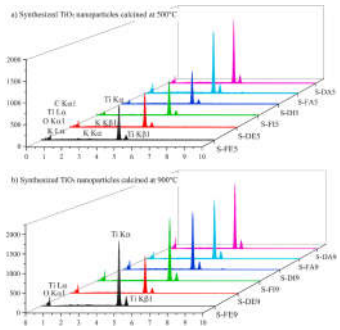

Fig. 3.6. EDS pattern of green TiO_2 nanoparticles calcined at 500 °C and 900 °C.

Table 3.2
Elemental mass and atomic percentage found in nanoparticles.

Nanoparticles	Calcination Temp. (°C)	Elements	Atomic %	Ratio of Ti:O
S-FE5	500	Ti	24.08	1: 2.42
		O	58.49	
		C	17.34	
		K	0.09	
S-FE9	900	Ti	31.86	1: 2.14
		O	68.14	
S-DE5	500	Ti	22.93	1: 2.78
		O	63.65	
		C	13.39	
		K	0.02	
S-DE9	900	Ti	24.51	1: 3.07
		O	75.49	
S-FI5	500	Ti	31.23	1: 1.86
		O	57.98	
		C	10.72	
		K	0.07	
S-FI9	900	Ti	29.03	1: 2.44
		O	70.97	
S-DI5	500	Ti	31.17	1: 1.90
		O	59.36	
		C	9.40	
		K	0.07	
S-DI9	900	Ti	29.33	1: 2.40
		O	70.67	
S-FA5	500	Ti	29.57	1: 1.95
		O	57.89	
		C	12.49	
		K	0.05	
S-FA9	900	Ti	34.69	1: 1.88
		O	65.31	
S-DA5	500	Ti	25.53	1: 2.38
		O	60.98	
		C	13.42	
		K	0.07	
S-DA9	900	Ti	28.97	1: 2.45
		O	71.03	

Tauc equation [3] $F(R)\ x\ h\nu = A\ (h\nu - Eg)^n$; (5)

Where, A is the proportionality constant, h is the Planck's constant (6.63×10^{-34} Js), n represents the type of transition. Since TiO_2 undergoes direct allowed transitions, a value of n = 2 was applied for determining the band gap of all the samples [56]. The evaluated band gap values for the prepared samples are shown in Fig. 3.10(c and d). The Tauc plots, which were used to determine the band gap energies, are shown in Fig. 3.7(c and d). The precise band gap value for each sample, as determined from these plots, is summarized alongside the Urbach energy in Table 3.4.

The band gap energies for the TiO_2 samples are summarized in Table 3.4, with values ranging from 3.18 to 3.31 eV for samples calcined at 500 °C, while those calcined at 900 °C exhibited band gap values in the range between 3.08 and 3.11 eV. These results were compared to the band gap of chemically synthesized pure TiO_2, which is approximately 3.22 eV [57]. The variation in band gap with higher calcination temperatures can be linked to alterations in the structural and electronic features of the nanoparticles [33]. At 500 °C, the green-synthesized nanoparticles exhibited a band gap close to that of pure TiO_2, indicating minimal surface modification or impurity incorporation from the neem leaf extract used in the synthesis [33]. Among the samples calcined at 500 °C, sample S-FE5 (fresh leaves, ethanol) exhibited a band gap energy of 3.18eV. This value, being close to that of pure TiO_2, suggests its potential for photo catalysis and applications where the intrinsic properties of TiO_2 are desired [58]. In this calcination temperature, the highest bandwidth gap was calculated to be 3.31 eV for the sample with dry neem leaves and isopropanol as an extraction solvent which might be due to fewer impurities and increased surface modification, suitable for UV protection, sensors, and UV-based devices [59]. To provide context for the functional potential of these materials, Table 3.5 summarizes published studies where TiO_2 nanoparticles with similar band gap energies have demonstrated strong photocatalytic activity. In contrast, a decrease and more consistency in the band gap was observed at 900 °C, likely due to increased crystallinity, particle growth, and the formation of oxygen vacancies at higher temperatures [60].

To assess the extent of disorder within the synthesized TiO_2 samples, the Urbach energy (Eu) was determined. Urbach energy (Eu) characterizes the extent of structural irregularities in nanoparticles, signifying localized states or defects within the optical band gap [61]. Urbach energy serves as an indicator of imperfections and non-uniformity within the crystal lattice, shedding light on the degree of lattice disruptions and structural inconsistencies. The Urbach energy was calculated using the following equation [62]:

$$\alpha = \alpha_0\, e^{\frac{h\nu}{Eu}}; \quad (6)$$

In this context, α denotes the absorption coefficient, α_0 is a constant, hν constitutes the energy of a photon (where h is Planck's constant and ν is the frequency), and Eu refers to the Urbach energy, which defines the exponential tail of the absorption spectrum.

The Urbach energy is computed from the slope of the linear region in the plot of ln (α) versus hν. The obtained values are shown in Fig. 3.11(a and b), with the specific values summarized in Table 3.4. The variations in Urbach energy values observed for the TiO_2 samples synthesized under different solvents and calcination conditions can be linked to differences in their structural characteristics, crystallinity, and defect densities.

The lower Urbach energy in samples synthesized with isopropanol suggests a more ordered structure, a finding consistent with the superior surface crystallinity observed in their Raman spectra. This could be explained by isopropanol's moderate polarity and slower evaporation rate, which may create a more consistent environment for nanoparticle formation, resulting in fewer structural imperfections [63]. This results in higher crystallinity, as also confirmed by sharper and more defined Raman peaks for these samples leading to lower Urbach energy.

Conversely, a potential reason for the higher Urbach energy in

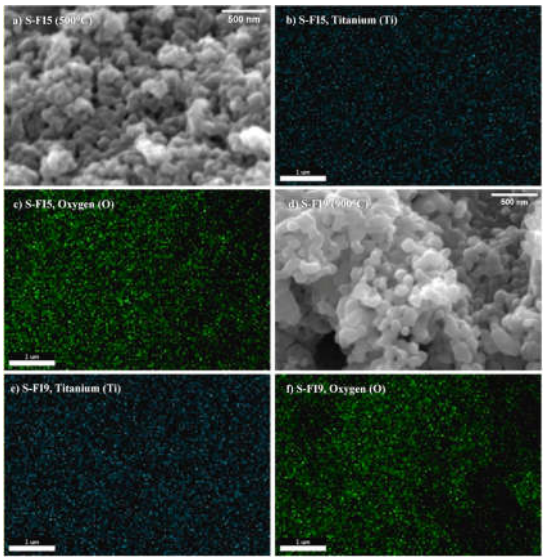

Fig. 3.7. EDS elemental mapping of representative nanoparticles. (a) SEM image of sample S-FI5 (500 °C) with its corresponding maps for (b) Titanium (Ti), (c) Oxygen (O); (d) SEM image of sample S-FI9 (900 °C) with its corresponding maps for (e) Titanium (Ti) and (f) Oxygen (O).

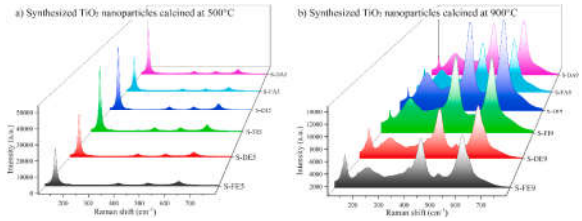

Fig. 3.8. Raman spectra of the nanoparticles calcined at; a) 500 °C and b) 900 °C.

ethanol-synthesized samples is ethanol's rapid evaporation rate and volatility, which could interfere with uniform nanoparticle growth and lead to more structural defects [64]. This trend is consistent with the broader Raman peaks observed for ethanol-synthesized samples, indicating lower crystallinity and greater lattice distortions.

The reduction in Urbach energy with rising calcination temperature

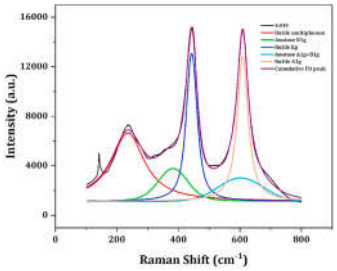

Fig. 3.9. Deconvoluted Raman spectrum of TiO_2 nanoparticles synthesized with fresh neem leaf, isopropanol solvent and calcined at 900 °C (S-FI9).

Table 3.3
Phase percentage found in nanoparticles calcined at 900 °C.

Nanoparticles	Peak position cm^{-1}	Intensity cm^{-1}	Phase	% Phase
S-FE9	142.108	4131.246	Anatase	36.73
	610.090	7115.773	Rutile	63.26
S-DE9	142.108	3734.698	Anatase	32.92
	610.090	7608.204	Rutile	67.07
S-FI9	142.108	1901.329	Anatase	14.63
	610.574	11089.820	Rutile	85.36
S-DI9	142.108	2268.081	Anatase	13.33
	610.574	14737.030	Rutile	86.66
S-FA9	142.628	3294.123	Anatase	26.75
	610.574	9017.486	Rutile	73.24
S-DA9	142.108	2840.143	Anatase	21.77
	610.090	10201.550	Rutile	78.22

can be attributed to improved crystallinity and a decrease in defect density at elevated temperatures [65]. At 900 °C, the increased thermal energy promotes grain growth, enhances particle packing, and repairs structural imperfections, thereby reducing localized states in the bandgap and lowering the Urbach energy [65]. Conversely, at 500 °C, crystallinity is less developed, and structural defects are more abundant, resulting in higher Urbach energy values [65]. This observation is corroborated by the Raman spectra, which display more distinct and pronounced peaks for samples calcined at 900 °C, reflecting better lattice organization and fewer defects.

3.6. Fourier transform infrared radiation (FTIR) analysis

Fourier-Transform Infrared (FTIR) spectroscopy was performed on the representative S-FE5 (fresh leaf, ethanol solvent, 500 °C) sample between 4000 and 400 cm^{-1} to assess its chemical structure (Fig. 3.12). The spectrum is dominated by a strong absorption peak at **627 cm^{-1}**, which is the characteristic vibrational mode of the Ti-O-Ti bonds, confirming the formation of a crystalline titanium dioxide network [3].

Interestingly, several other bands are also present. A broad band is centered at **3239 cm^{-1}**, which is attributed to the O-H stretching vibrations of water molecules adsorbed onto the nanoparticle surface from the atmosphere [69]. A sharp, prominent peak is visible at **1661 cm^{-1}**, which can be assigned to the bending mode of these adsorbed water molecules, though its intensity may also suggest the presence of residual C=O (carbonyl) groups from the phytochemical capping agents [70]. Other weaker bands associated with organic material are also observed at **2585 cm^{-1}** and **1057 cm^{-1}** (corresponding to C-O stretching) [69].

3.7. Analysis of reaction yield

The percentage yield of the synthesized TiO_2 nanoparticles was calculated to assess the efficiency of the green synthesis process. Based on the initial amount of the titanium precursor (5 mL of TTIP), the theoretical maximum yield of pure TiO_2 is 1.35 g. The actual mass of the final powder after calcination was consistently around 1.2 g for all samples, corresponding to an approximate yield of **88.9 %**.

Interestingly, the parameters varied in this study—leaf condition (fresh vs. dry) and solvent type (ethanol, isopropanol, acetonitrile)—did not have a significant impact on the final yield. This suggests that the quantity of the limiting reactant, titanium isopropoxide, is the dominant factor controlling the overall yield, while the different solvents and extract conditions are all capable of providing sufficient phytochemicals for the reaction to proceed to near completion. Therefore, the primary influence of the studied parameters is on the final physical and optical properties of the nanoparticles rather than the efficiency of their production.

4. Conclusion

This research highlights the efficiency of green synthesis using neem leaf extract as an eco-conscious and green approach for producing TiO_2 nanoparticles through leveraging both fresh and dry neem leaves with ethanol, isopropanol, and acetonitrile solvents, subsequently subjected to calcination at 500 °C and 900 °C. The formed nanoparticles exhibited diverse structural, morphological, and optical properties, demonstrating the versatility of this synthesis approach. This systematic comparison moves beyond a simple proof-of-concept to provide a strategic framework for predictably tuning nanoparticle properties, such as achieving 100 % phase purity for either anatase or rutile. A comparison of XRD and Raman spectroscopy results revealed differences in the assessment of crystallinity. XRD analysis showed that samples calcined at 500 °C with fresh neem leaves and ethanol solvent had the highest bulk crystallinity. However, Raman spectroscopy and Urbach energy analysis identified samples synthesized with isopropanol and fresh neem leaves as having superior surface crystallinity and lower structural disorder. As Raman spectroscopy is more sensitive to surface characteristics, it offers more detailed insights into localized crystallinity, which is essential for applications reliant on surface activity. This key finding demonstrates that bulk and surface properties can be independently tuned, providing a strategic choice for optimizing nanoparticles for either structural or surface-dependent applications. This elucidation of the links between solvent choice, bulk/surface crystallinity, and structural disorder provides foundational mechanistic insights into the role of phytochemical interactions during synthesis. SEM analysis revealed pseudo-spherical morphologies, with particle sizes ranging from 75 to 80 nm for samples calcined at 500 °C and 80–95 nm for those calcined at 900 °C. These relatively small, uniform particle sizes enhance surface area, a key feature for potential catalytic and adsorption applications. EDS analysis confirmed the high purity of the synthesized nanoparticles, with an atomic Ti:O ratio consistently close to the ideal stoichiometric value of 1:2. This composition ensures the structural stability and reliability of the nanoparticles, which are important factors for their potential use in photocatalytic and optical applications. UV-DRS analysis demonstrated band gap energies of 3.18–3.31 eV for samples calcined at 500 °C, aligning closely with the band gap of TiO_2. As shown in Table 3.5, these values are consistent with those of materials proven to be effective in photocatalytic applications, which strongly supports the potential of our sustainably synthesized nanoparticles. For samples calcined at 900 °C, the band gap narrowed to 3.08–3.11 eV, indicative of enhanced crystallinity and the formation of oxygen vacancies, which improve light absorption for specific applications. Overall, the synthesis conditions played a pivotal role in shaping the structural, photonic, and

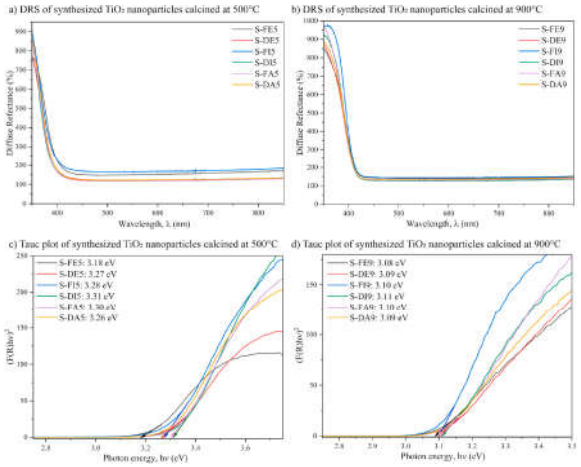

Fig. 3.10. (a), (b) UV–Vis DRS spectra and (c), (d) Tauc plot of green TiO_2 synthesized at different condition and calcined at 500 °C (a,b) and 900 °C (c,d).

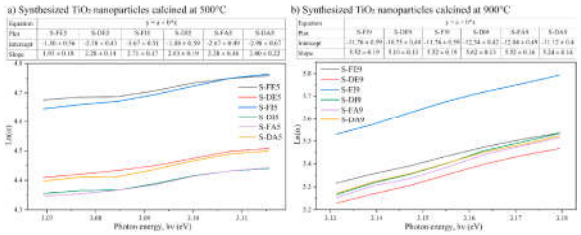

Fig. 3.11. Urbach energy of the nano particles calcined at a) 500 °C and b) 900 °C.

morphological traits of the TiO_2 nanoparticles. By demonstrating a sustainable pathway to high-purity materials with features optimized for specific end-uses, this work enhances the application-readiness of green-synthesized nanoparticles. This study underscores the potential of neem leaf extract as an efficient and sustainable reducing and stabilizing agent, advancing green chemistry approaches to scalable nanomaterial production. The dual-phase synthesis, yielding both anatase and rutile phases, highlights the versatility of these nanoparticles suggesting their potential for a comprehensive array of commercial, green, and clinical deployment.

CRediT authorship contribution statement

Nusrat Zahan: Writing – original draft, Visualization, Investigation, Formal analysis. **Md Rashed Alam:** Investigation, Formal analysis. **Munira Sultana:** Validation, Investigation, Formal analysis. **Afrina Sharmin:** Writing – review & editing, Visualization. **Shahran Ahmed:** Visualization. **Sharmin Jahan:** Formal analysis. **M.S. Bashar:** Writing – review & editing, Supervision, Resources, Project administration, Methodology, Funding acquisition, Conceptualization.

Table 3.4
Optical parameters of the nanoparticles calcined at 500 °C and 900 °C.

Sample	Calcination Temp. (°C)	Bandgap (eV)	Urbach energy (meV)
S-FE5	500	3.18	513.79 ± 4.53
S-FE9	900	3.08	181.05 ± 0.21
S-DE5	500	3.27	439.30 ± 1.62
S-DE9	900	3.09	195.95 ± 0.12
S-FI5	500	3.28	369.33 ± 1.38
S-FI9	900	3.10	177.87 ± 0.10
S-DI5	500	3.31	493.05 ± 4.43
S-DI9	900	3.11	181.05 ± 0.21
S-FA5	500	3.30	437.87 ± 2.12
S-FA9	900	3.10	181.00 ± 0.15
S-DA5	500	3.26	416.53 ± 3.43
S-DA9	900	3.09	190.98 ± 0.13

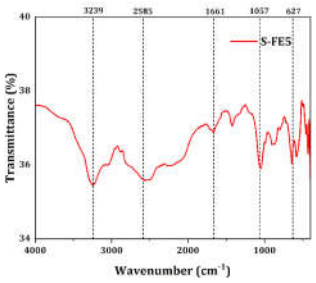

Fig. 3.12. FTIR spectra for TiO_2 synthesized with fresh neem leaf, ethanol solvent and calcined at 500 °C (S-FE5).

Table 3.5
Representative photocatalytic applications of TiO_2 with band gaps corresponding to the synthesized samples.

Band Gap (eV)	Crystal Phase	Photocatalytic Application	Key Finding/ Performance	Reference
3.18–3.31	Anatase	Dye Degradation (UV Light)	Degraded over 90 % of Methylene Blue dye under UV irradiation in 120 min.	[66,67]
3.18–3.22	Anatase	Antibacterial Activity	Showed significant activity against *E. coli* and *S. aureus* under UV light via the generation of reactive oxygen species (ROS).	[67]
~3.05	Rutile	Pollutant Degradation (Visible Light)	When doped or surface-modified, the lower band gap allows for the degradation of various pollutants under visible light irradiation.	[68]

Data availability statement

The dataset generated for analysis during the current study is available from the corresponding author on reasonable request.

Declaration of competing interest

The authors declare that they have no known competing financial interests or personal relationships that could have appeared to influence the work reported in this paper.

Acknowledgements

The Bangladesh Council of Scientific and Industrial Research (BCSIR)'s Institute of Energy Research and Development (IERD) is acknowledged by the authors for all of the support it provided with this research work. The research and development project funding plan of the Bangladesh Council of Scientific and Industrial Research (BCSIR), Ministry of Science and Technology, Bangladesh, provides guidance for this effort. (ref: February 39, 0000.011.14.157.2022.172; Dt- November 10, 2022) entitled 'Study on Optoelectronic Semiconductor Devices'.

References

[1] M. Aravind, M. Amalanathan, M.S.M. Mary, Synthesis of TiO2 nanoparticles by chemical and green synthesis methods and their multifaceted properties, SN Appl. Sci. 3 (4) (2021) 1–10, https://doi.org/10.1007/s42452-021-04281-5.
[2] V. Verma, M. Al-Dossari, J. Singh, M. Rawat, M.G.M. Kordy, M. Shaban, A review on green synthesis of TiO2 NPs: synthesis and applications in photocatalysis and antimicrobial, Polymers 14 (7) (2022), https://doi.org/10.3390/polym14071444.
[3] N. Zahan, S.A. Fahim, M.S.H. Shuvo, M. Sarker, S.M. Masum, M.A.I. Molla, Fabrication and characterization of C-doped TiO2 nanoparticles for the photodegradation of organic dyes, Inorganic and Nano-Metal Chemistry 0 (0) (2024) 1–13, https://doi.org/10.1080/24701556.2024.2355506.
[4] P. Singh Jassal, D. Kaur, R. Prasad, J. Singh, Green synthesis of titanium dioxide nanoparticles: development and applications, J. Agric. Food Res. 10 (May) (2022) 100361, https://doi.org/10.1016/j.jafr.2022.100361.
[5] I. Khan, K. Saeed, I. Khan, Nanoparticles: properties, applications and toxicities, Arab. J. Chem. 12 (7) (Nov. 2019) 908–931, https://doi.org/10.1016/J.ARABJC.2017.05.011.
[6] D. Yang, D. Yang, Titanium Dioxide - Material for a Sustainable Environment, Titanium Dioxide - Material for a Sustainable Environment, Jun. 2018, https://doi.org/10.5772/INTECHOPEN.70290.
[7] A. Fujishima, X. Zhang, D.A. Tryk, TiO2 photocatalysis and related surface phenomena, Surf. Sci. Rep. 63 (12) (Dec. 2008) 515–582, https://doi.org/10.1016/J.SURFREP.2008.10.001.
[8] S. Challagulla, S. Roy, The role of fuel to oxidizer ratio in solution combustion synthesis of TiO2and its influence on photocatalysis, J. Mater. Res. 32 (14) (2017) 2764–2772, https://doi.org/10.1557/jmr.2017.244.
[9] S.A. Fahim, N. Zahan, R.A. Shathy, M. Moniruzzaman, Materials chemistry and physics, Mater. Chem. Phys. 75 (1–3) (2002), https://doi.org/10.1016/0254-0584(95)01496-9.
[10] L. Huang, T. Liu, H. Zhang, W. Guo, W. Zeng, Hydrothermal synthesis of different TiO2 nanostructures: structure, growth and gas sensor properties, J. Mater. Sci. Mater. Electron. 23 (11) (2012) 2024–2029, https://doi.org/10.1007/s10854-012-0697-6.
[11] S. Arab, D. Li, N. Kinsinger, F. Zaera, D. Kisailus, Solvothermal synthesis of a highly branched Ta-doped TiO2, J. Mater. Res. 26 (20) (2011) 2653–2659, https://doi.org/10.1557/jmr.2011.286.
[12] K.L. Ou, et al., Titanium dioxide electron-selective interlayers created by chemical vapor deposition for inverted configuration organic solar cells, J Mater Chem A Mater 1 (23) (2013) 6794–6803, https://doi.org/10.1039/c3ta10894e.
[13] V. Patidar, P. Jain, Green synthesis of TiO2 nanoparticle using Moringa Oleifera leaf extract, International Research Journal of Engineering and Technology (2017) 470–474 [Online]. Available: www.irjet.net.
[14] G. Kianpour, M. Salavati-Niasari, H. Emadi, Sonochemical synthesis and characterization of NiMoO4 nanorods, Ultrason. Sonochem. 20 (1) (2013) 418–424, https://doi.org/10.1016/j.ultsonch.2012.08.012.
[15] F. Mohandes, M. Salavati-Niasari, Sonochemical synthesis of silver vanadium oxide micro/nanorods: solvent and surfactant effects, Ultrason. Sonochem. 20 (1) (2013) 354–365, https://doi.org/10.1016/j.ultsonch.2012.05.002.
[16] M. Amiri, A. Pardakhti, M. Ahmadi-Zeidabadi, A. Akbari, M. Salavati-Niasari, Magnetic nickel ferrite nanoparticles: green synthesis by Urtica and therapeutic effect of frequency magnetic field on creating cytotoxic response in neural cell lines, Colloids Surf. B Biointerfaces 172 (Dec. 2018) 244–253, https://doi.org/10.1016/j.colsurfb.2018.08.049.
[17] P.K. Dikshit, et al., Green Synthesis of Metallic Nanoparticles: Applications and Limitations, 2021, https://doi.org/10.3390/catal11080902.
[18] A.I. Osman, et al., Synthesis of green nanoparticles for energy, biomedical, environmental, agricultural, and food applications: a review, Environ. Chem. Lett. 22 (2) (2024) 841–887, https://doi.org/10.1007/s10311-023-01682-3.
[19] M. Salavati-Niasari, F. Davar, M.R. Loghman-Estarki, Controllable synthesis of thioglycolic acid capped ZnS(Pn)0.5 nanotubes via simple aqueous solution route at low temperatures and conversion to wurtzite ZnS nanorods via thermal

decompose of precursor, J. Alloys Compd. 494 (1–2) (Apr. 2010) 199–204, https://doi.org/10.1016/j.jallcom.2009.10.265.

[20] M. Salavati-Niasari, F. Davar, M.R. Loghman-Estarki, Controllable synthesis of thioglycolic acid capped ZnS(Pn)0.5 nanotubes via simple aqueous solution route at low temperatures and conversion to wurtzite ZnS nanorods via thermal decompose of precursor, J. Alloys Compd. 494 (1–2) (Apr. 2010) 199–204, https://doi.org/10.1016/j.jallcom.2009.10.265.

[21] H. Kaur, S. Kaur, S. Kumar, J. Singh, M. Rawat, Eco-friendly approach: synthesis of novel green TiO2 nanoparticles for degradation of reactive green 19 dye and replacement of chemical synthesized TiO2, J. Cluster Sci. 32 (5) (2021) 1191–1204, https://doi.org/10.1007/s10876-020-01881-w.

[22] M. Sundrarajan, S. Gowri, Green synthesis of titanium dioxide nanoparticles by nyctanthes arbor-tristis leaves extract 8 (8) (2011) 447–451.

[23] S. Pratap, G. Saxena, V. Singh, A. Kumar, Green synthesis of TiO 2 nanoparticles using leaf extract of Jatropha curcas L . for photocatalytic degradation of tannery wastewater, Chem. Eng. J. 336 (2018) 386–396, https://doi.org/10.1016/j.cej.2017.12.029. September 2017.

[24] J. Rajkumari, et al., Journal of photochemistry & photobiology , B : biology synthesis of titanium oxide nanoparticles using Aloe barbadensis miill and evaluation of its antibiofilm potential against Pseudomonas aeruginosa PAO1, J. Photochem. Photobiol., B 201 (2019) 111667, https://doi.org/10.1016/j.jphotobiol.2019.111667. August.

[25] T. Santhoshkumar, et al., Green synthesis of titanium dioxide nanoparticles using Psidium guajava extract and its antibacterial and antioxidant properties, Asian Pac. J. Tropical Med. 7 (12) (2014) 968–976, https://doi.org/10.1016/S1995-7645(14)60171-1.

[26] M. Behpour, S.M. Ghoreishi, A. Gandomi-Niasar, N. Soltani, M. Salavati-Niasari, The inhibition of mild steel corrosion in hydrochloric acid media by two Schiff base compounds, J. Mater. Sci. 44 (10) (May 2009) 2444–2453, https://doi.org/10.1007/s10853-009-3309-y.

[27] Sol-gel science | ScienceDirect [Online]. Available: https://www.sciencedirect.com/book/9780080571034/sol-gel-science?via=ihub=. (Accessed 3 July 2025).

[28] L. Velardi, L. Scrimieri, A. Serra, D. Manno, L. Calcagnile, Effect of temperature on the physical, optical and photocatalytic properties of TiO2 nanoparticles, SN Appl. Sci. 2 (4) (2020) 1–6, https://doi.org/10.1007/s42452-020-2544-3.

[29] Y. Zhang, J. Chen, X. Li, Preparation and photocatalytic performance of anatase/rutile mixed-phase TiO2 nanotubes, Catal. Lett. 139 (3) (2010) 129–133, https://doi.org/10.1007/s10562-010-0425-x.

[30] R. Das, V. Ambardekar, P.P. Bandyopadhyay, in: Titanium Dioxide, H.M. Ali (Eds.), Titanium Dioxide and its Applications in Mechanical, Electrical, Optical, and Biomedical Fields, IntechOpen, Rijeka, 2021, https://doi.org/10.5772/intechopen.98805 ch. 7.

[31] R.W.G. Wyckoff, Crystal Structures - Volume 1, second ed., New York SE - 467 ε Interscience Publishers, 1963. LK, https://worldcat.org/title/473923608.

[32] E.P. Meagher, G.A. Lager, Polyhedral thermal expansion in the TiO2 polymorphs; refinement of the crystal structures of rutile and brookite at high temperature, Can. Mineral. 17 (1) (1979) 77–85.

[33] Z.N. Kayani, F. Saleemi, I. Batool, Effect of calcination temperature on the properties of ZnO nanoparticles, Appl. Phys. A 119 (2) (2015) 713–720, https://doi.org/10.1007/s00339-015-9019-1.

[34] Y. Li, X. Wang, L. Ding, Y. Li, R. He, J. Li, Changing the calcination temperature to tune the microstructure and polishing properties of ceria octahedrons, RSC Adv. 12 (26) (2022) 16554–16560, https://doi.org/10.1039/d2ra02367a.

[35] K. Chand, et al., Green synthesis characterization and antimicrobial activity against: staphylococcus aureus of silver nanoparticles using extracts of neem, onion and tomato, RSC Adv. 9 (30) (2019) 17002–17015, https://doi.org/10.1039/c9ra01407a.

[36] P. Senthilkumar, S. Rashmitha, P. Veera, C. Vijay Ignatious, C. SaiPriya, A. V. Samrot, Antibacterial activity of neem extract and its green synthesized silver nanoparticles against pseudomonas aeruginosa, J. Pure Appl. Microbiol. 12 (2) (2018) 969–974, https://doi.org/10.22207/JPAM.12.2.60.

[37] M. Shiraz, H. Imtiaz, A. Azam, S. Hayat, Phytogenic nanoparticles: synthesis, characterization, and their roles in physiology and biochemistry of plants, Biometals 37 (1) (2024) 23–70, https://doi.org/10.1007/s10534-023-00542-5.

[38] A. Sharma, S. Kumar, in: H.M. Lal, S. Thomas, T. Li, H.J. Maria (Eds.), Synthesis and Green Synthesis of Silver Nanoparticles BT - Polymer Nanocomposites Based on Silver Nanoparticles: Synthesis, Characterization and Applications, Springer International Publishing, Cham, 2021, pp. 25–64, https://doi.org/10.1007/978-3-030-44259-0_2.

[39] G. Rajakumar, A.A. Rahuman, B. Priyamvada, V.G. Khanna, D.K. Kumar, P.J. Sujin, Eclipta prostrata leaf aqueous extract mediated synthesis of titanium dioxide nanoparticles, Mater. Lett. 68 (Feb. 2012) 115–117, https://doi.org/10.1016/J.MATLET.2011.10.038.

[40] C. Dhand, et al., Methods and strategies for the synthesis of diverse nanoparticles and their applications: a comprehensive overview, RSC Adv. 5 (127) (Dec. 2015) 105003–105037, https://doi.org/10.1039/C5RA19388E.

[41] V. Mote, Y. Purushotham, B. Dole, Williamson-hall analysis in estimation of lattice strain in nanometer-sized ZnO particles, Journal of Theoretical and Applied Physics 6 (1) (Dec. 2012), https://doi.org/10.1186/2251-7235-6-6.

[42] I. Khan, K. Saeed, I. Khan, Nanoparticles: properties, applications and toxicities, Arab. J. Chem. 12 (7) (2019) 908–931, https://doi.org/10.1016/j.arabjc.2017.05.011.

[43] W. Jiang, B.Y.S. Kim, J.T. Rutka, W.C.W. Chan, Nanoparticle-mediated cellular response is size-dependent, Nat. Nanotechnol. 3 (3) (2008) 145–150, https://doi.org/10.1038/nnano.2008.30.

[44] J. Pérez-Juste, I. Pastoriza-Santos, L.M. Liz-Marzán, P. Mulvaney, Gold nanorods: synthesis, characterization and applications, Coord. Chem. Rev. 249 (17–18) (2005) 1870–1901, https://doi.org/10.1016/j.ccr.2005.01.030. SPEC. ISS.

[45] D.W. Boukhvalov, V. Paolucci, Catalysis , Gas Sensing , adsorption-assisted and Challenges for Surface Science, 2021, pp. 7541–7552, https://doi.org/10.1039/d0cp03117k.

[46] S.S. Mohtar, et al., Impact of Doping and Additive Applications on Photocatalyst Textural Properties in Removing Organic Pollutants : a Review, 2021, pp. 1–31.

[47] R. Javed, M. Zia, S. Naz, S.O. Aisida, N. ul Ain, Q. Ao, Role of capping agents in the application of nanoparticles in biomedicine and environmental remediation: recent trends and future prospects, J. Nanobiotechnol. 18 (1) (2020) 172, https://doi.org/10.1186/s12951-020-00704-4.

[48] A. Orlando, et al., A comprehensive review on Raman spectroscopy applications, Chemosensors 9 (9) (2021), https://doi.org/10.3390/chemosensors9090262.

[49] P. Argüelles-Lucho, R. Pérez-Cuapio, R.M. Woo-García, L. García-González, M. Pacio, F. López-Huerta, TiO2 synthesis anatase phase with the sol-gel process at room temperature, IOP Conf. Ser. Mater. Sci. Eng. 908 (2020) [Online]. Available: https://api.semanticscholar.org/CorpusID:225388134.

[50] C.M. Mbulanga, et al., Raman spectroscopy characterisation of oriented bundles of single-crystal rutile-phase TiO2 nanorods prepared by hydrothermal bath deposition on transparent conducting substrates, Appl. Phys. A 125 (2019) 1–10 [Online]. Available: https://api.semanticscholar.org/CorpusID:165091507.

[51] A.R. Zanatta, A fast-reliable methodology to estimate the concentration of rutile or anatase phases of TiO2, AIP Adv. 7 (7) (2017), https://doi.org/10.1063/1.4992130.

[52] Y. Su, J. Xue, A. Liu, T. Ma, L. Gao, Unveiling the effect of solvents on crystallization and morphology of 2D perovskite in solvent-assisted method, Molecules 27 (6) (2022), https://doi.org/10.3390/molecules27061828.

[53] A. Pandey, S. Dalal, S. Dutta, A. Dixit, Structural characterization of polycrystalline thin films by X-ray diffraction techniques, J. Mater. Sci. Mater. Electron. 32 (2) (2021) 1341–1368, https://doi.org/10.1007/s10854-020-04998-w.

[54] T. Kinsella, Surface analysis, Med. Device Technol. 17 (8) (2006) 39–40, https://doi.org/10.4011/shikizai1937.76.204.

[55] Harrick Scientific Products, What is kubelka-munk [Online]. Available, http://mmrc.caltech.edu/FTIR/Literature/Kubelka-Munk.pdf, 2017.

[56] A. Singh, B.K. Mishra, Removal of chlorhexidine digluconate from aqueous solution by heterogenous photocatalysis using sunlight-driven Ni-doped TiO2 material, Environ. Eng. Res. 28 (1) (Feb. 2023) 210540–210546, https://doi.org/10.4491/eer.2021.546.

[57] P. Makuła, M. Pacia, W. Macyk, How to correctly determine the band gap energy of modified semiconductor photocatalysts based on UV–Vis spectra, J. Phys. Chem. Lett. 9 (23) (Dec. 2018) 6814–6817, https://doi.org/10.1021/acs.jpclett.8b02892.

[58] M. Mhadhbi, H. Abderrazzak, B. Avar, Synthesis and properties of titanium dioxide nanoparticles, in: B. Bejaoui (Ed.), Updates on Titanium Dioxide, IntechOpen, Rijeka, 2023, https://doi.org/10.5772/intechopen.111577 ch. 5.

[59] M. Isik, S. Delice, N. Gasanly, Temperature-dependent optical properties of TiO2 nanoparticles: a study of band gap evolution, Opt. Quant. Electron. 55 (10) (2023) 905, https://doi.org/10.1007/s11082-023-05138-4.

[60] J. Singh, G.P. Singh, R.K. Jain, B. Singh, K.J. Singh, R.C. Singh, Effect of calcination temperature on structural, optical and antibacterial properties of ball mill synthesized Co3O4 nanomaterials, J. Mater. Sci. Mater. Electron. 33 (6) (2022) 3250–3266, https://doi.org/10.1007/s10854-021-07526-6.

[61] A. Sharmin, S.S. Mahmood, M. Sultana, S. Aziz, M.A.A. Shaikh, M.S. Bashar, Effect of argon pressure on the physical characteristics of cadmium telluride (CdTe) thin films by close-spaced sublimation, J. Mater. Sci. Mater. Electron. 34 (5) (2023), https://doi.org/10.1007/s10854-022-09603-w.

[62] O. Applications, et al., A study of the optical properties and urbach tail of spray-deposited TiO_2 thin films at different volumes for. www.anu.com, 2024.

[63] N. Fifere, R. Ardeleanu, F. Doroftei, M. Dobromir, A. Airinei, Tailoring the structural and optical properties of cerium oxide nanoparticles prepared by an ecofriendly green route using plant extracts, Int. J. Mol. Sci. 25 (1) (2024), https://doi.org/10.3390/ijms25010681.

[64] H.S. Kim, et al., Ethanol purification enables high-quality α-phase $FAPbI_3$ perovskite microcrystals for commercial photovoltaic applications, Nanoscale Horiz 9 (7) (2024) 1120–1127, https://doi.org/10.1039/D4NH00061G.

[65] A. Amato, et al., Observation of a correlation between internal friction and urbach energy in amorphous oxides thin films, Sci. Rep. 10 (1) (2020) 1670, https://doi.org/10.1038/s41598-020-58380-1.

[66] I.K. Konstantinou, T.A. Albanis, TiO2-assisted photocatalytic degradation of azo dyes in aqueous solution: kinetic and mechanistic investigations: a review, Appl. Catal., B 49 (1) (Apr. 2004) 1–14, https://doi.org/10.1016/J.APCATB.2003.11.010.

[67] H.A. Foster, I.B. Ditta, S. Varghese, A. Steele, Photocatalytic disinfection using titanium dioxide: spectrum and mechanism of antimicrobial activity, Appl. Microbiol. Biotechnol. 90 (6) (Apr. 2011) 1847–1868, https://doi.org/10.1007/S00253-011-3213-7, 2011 90:6.

[68] M. Pelaez, et al., A review on the visible light active titanium dioxide photocatalysts for environmental applications, Appl. Catal., B 125 (Aug. 2012) 331–349, https://doi.org/10.1016/J.APCATB.2012.05.036.

[69] Introduction to spectroscopy, 5th edition : free download, borrow, and streaming : internet archive [Online]. Available: https://archive.org/details/IntroductionToSpectroscopy5thEdition. (Accessed 3 July 2025).

[70] M. Khan, et al., Green synthesis of silver nanoparticles mediated by Pulicaria glutinosa extract, Int. J. Nanomed. 8 (Apr. 2013) 1507–1516, https://doi.org/10.2147/IJN.S43309.